Journal of Power Sources 251 (2014) 363–369

Contents lists available at ScienceDirect

Journal of Power Sources

journal homepage: www.elsevier.com/locate/jpowsour

Synergy among manganese, nitrogen and carbon to improve the catalytic activity for oxygen reduction reaction

Jian Kang [a], Hui Wang [a], Shan Ji [b,*], Julian Key [b], Rongfang Wang [a,*]

[a] Key Laboratory of Eco-Environment-Related Polymer Materials, Ministry of Education of China, College of Chemistry and Chemical Engineering, Northwest Normal University, Lanzhou 730070, China
[b] South African Institute for Advanced Materials Chemistry, University of the Western Cape, Cape Town 7535, South Africa

HIGHLIGHTS

- Mn-N dual doped carbon, e.g. Mn-CN_x, was prepared.
- Mn-CN_x showed good catalytic activity for oxygen reduction reaction.
- Synergy among Mn, N and C results in the enhanced activity of Mn-CN_x.

ARTICLE INFO

Article history:
Received 4 September 2013
Received in revised form
13 November 2013
Accepted 18 November 2013
Available online 28 November 2013

Keywords:
Manganese-modified
Nitrogen-doped carbon
Glycine
Oxygen reduction reaction

ABSTRACT

A highly active electrocatalyst for oxygen reduction reaction, manganese modified glycine derivative-carbon (Mn-CN_x), is synthesized by a two-step carbonizing process. X-ray diffraction, Raman spectroscopy, and X-ray photoelectron spectroscopy are used to characterize structure and morphology of the catalysts. Electrochemical tests show that Mn-CN_x has higher catalytic activity for oxygen reduction reaction than CN_x derived glycine and Mn modified Vulcan carbon. Moreover, the half-wave potential of Mn-CN_x is only 12 mV lower than that of commercial Pt/C. Mn-CN_x also has excellent durability to methanol crossover in alkaline solution, and thus provides a promising low cost, non-precious metal cathode catalyst for fuel cells.

1. Introduction

The oxygen reduction reaction (ORR) is the dominant factor affecting the overall performance of proton exchange fuel cells (PEMFCs) as it is kinetically the slowest process [1–4]. In order to accelerate the ORR, high loadings of platinum are required on the cathode, which make PEMFCs too expensive for competitive commercialization [5,6]. Besides the high cost of Pt, the Pt-based electrocatalysts still face a series of challenges, such as low selectivity and poor durability [7]. Therefore, development of platinum-free [8,9], non-noble metal catalysts [10–12] and metal-free catalysts [13–17] which could be more efficient, durable, and less expensive than Pt-based catalysts has attracted much attention [18].

Among these Pt-free catalysts, nitrogen-doped carbon materials are attractive as potential ORR catalysts because they not only exhibit excellent electrocatalytic ORR activity but also have advantages, such as low cost, long durability, and environmental friendliness [13,15,16,19–21]. In particular, the pyridinic-N and graphitic-N type of nitrogen-doped carbon are quite active in ORR [22]. In pyridinic-N and graphitic-N, nitrogen atoms bond to two carbon atoms at the edges of the graphite planes, and with the three carbon atoms within the graphite (basal) plane. Nitrogen donates an electron from its electron pair to the π-conjugated bond system, imparting Lewis basic sites to the carbon and enabling the carbon to adsorb molecular oxygen and then transfer this electron to molecular oxygen to form intermediates, such as OH^-, O_2, and HO_2^- [23–25]. However, while nitrogen clearly plays an important role in ORR on nitrogen-doped carbons materials, the ORR activity of most N-doped carbons is still not competitive to Pt-based catalysts.

In the last century, it has been reported that the alloys between Pt and Mn had better catalytic activity for ORR than Pt/C due to the

* Corresponding authors.
E-mail addresses: sji@uwc.ac.za (S. Ji), wrf38745779@126.com, wangrf@nwnu.edu.cn (R. Wang).

0378-7753/$ – see front matter © 2013 Elsevier B.V. All rights reserved.
http://dx.doi.org/10.1016/j.jpowsour.2013.11.045

electronic and geometric factors [26]. Kang et al. prepared cubic PtMn nanocrystals and studied its activity for ORR [27]. The MnPt nanocubes show higher ORR activity than the commercial catalyst in acid solution. Recently, the effect of Mn addition on the promotion of ORR activity of PtCo/C catalyst was also studied [28]. Furthermore, Jia et al. studied the relationships between the atomic structure, electronic property and ORR activity of Pt_3M nanoparticles including Pt_3Mn by the modeling approach and experimental [29]. These work demonstrated that Mn could enhance the activity of Pt for ORR in acid solution.

On the other hand, various manganese oxides (MnO_x), including MnO_2, MnO, Mn_2O_3, Mn_3O_4, Mn_5O_8, MnOOH, and amorphous MnO_x have been studied as ORR catalysts in alkaline solutions, due to their low cost and minimum environmental impact [30–33]. However, pristine MnO_x usually exhibits limited ORR activity due to its low electrical conductivity. Nevertheless, loading of MnO_x on conducting carbon carriers significantly improves the electrical conductivity and ORR activity, and a carbon-supported, nano-sized, manganese oxide, synthesized via a chemical depositional method, has been reported to produce relatively high ORR activity in alkaline KOH solutions [34]. Since nitrogen-doped carbon shows some metal-like behavior, we envisioned that the ORR activity of MnO_x could be further enhanced by depositing it on nitrogen-doped carbon to exploit a synergetic coupling between the two materials.

In this study, a facile, environmental friendly method has been developed to produce manganese-modified, nitrogen-doped, carbon (Mn-CN_x) by first carbonizing glycine followed by further heat-treatment with manganese salts under N_2 atmosphere. Glycine is a naturally abundant material with high nitrogen content, and thus a promising source material for preparing nitrogen-doped carbon. The resultant morphology and electrocatalytic properties of the above synthesized materials are reported here with results showing that the Mn-CN_x catalyst has similar electrocatalytic ORR activity to commercial Pt/C and has high methanol tolerance.

2. Experimental

2.1. Preparation of manganese modified nitrogen-doped carbon

Manganese modified nitrogen-doped carbon was prepared by two-step heat treatment process. An aqueous solution (50 mL) containing glycine (2.0 g) and potassium chloride (KCl, 2.0 g) was stirred for 0.5 h, and then the water was removed from the solution by heating at 353 K. The obtained mixture was carbonized at 1073 K under N_2 atmosphere for 2 h. The resultant product was ground with a ball mill, and then washed with ultrapure water until no chlorine ions were detected. The nitrogen-doped carbon made from glycine was recovered by drying at 333 K for 6 h in an oven. Potassium permanganate ($KMnO_4$) (300 mg) was then dissolved in 20 mL ultrapure water to which the prepared nitrogen-doped carbon (500 mg) was then added and sonicated for 20 min. The solution was dried in a vacuum oven at 333 K and the obtained powder was ball-milled and finally heat-treated at 1073 K under N_2 atmosphere for 2 h. For comparison, manganese modified Vulcan XC-72 carbon (Mn–C) and undoped-Mn carbon derived glycine (CN_x) was prepared using similar procedure to that described above.

2.2. Characterization

The Mn-CN_x was characterized by recording their X-ray diffraction (XRD) patterns on a Shimadzu XD-3A (Japan), using filtered Cu-Kα radiation (40 kV, 30 mA). X-ray photoelectron spectra (XPS) was obtained using a VG Escalab210 spectrometer fitted with Mg 300 W X-ray source, and accurate binding energies were determined by referencing to the C 1s peak at 284.8 eV. Scanning electron microscopy (SEM) images were carried out on a Carl Zeiss Ultra Plus microscope. Raman spectra were obtained on a Ft-Raman spectroscopy (RFS 100, BRU-KER) employing Nd: YAG laser wavelength of 1064 nm.

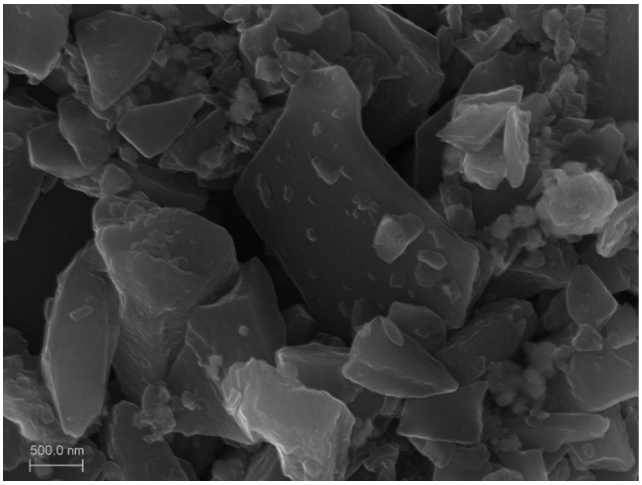

Fig. 1. SEM of Mn-CN_x.

The electrochemical measurements for ORR were carried out on a CHI650D electrochemical work station at 303 K using a three-electrode system with 0.1 M KOH as an electrolyte. For cyclic voltammetric (CV) measurements, a 5 mm diameter glassy carbon disk working electrode was used. Linear sweep voltammetry (LSV) was recorded at a scan rate of 5 mV s^{-1} with a rotating glassy carbon disk electrode (RDE, 5 mm in diameter) as the working electrode, and the rotation rate of the disk was varied between 400 and 2500 rpm. To prepare the working electrode, 5.0 mg of catalyst was dispersed ultrasonically in 1 mL of diluted Nafion alcohol solution (0.25% Nafion) for 10 min, and 8 μL of the suspension was pipetted piped onto a glassy carbon substrate. Pt wire was used as the counter electrode. The reference electrode was an Ag/AgCl (3 M KCl) electrode in the same electrolyte as the electrochemical cell. Unless otherwise specified, the loading of the catalysts in all electrochemical test in this work is ca. 0.204 mg cm^{-2}. Prior to measurement, O_2 was bubbled directly into the cell for at least 15 min to saturate the solution. During each measurement, O_2 was flushed over the cell solution.

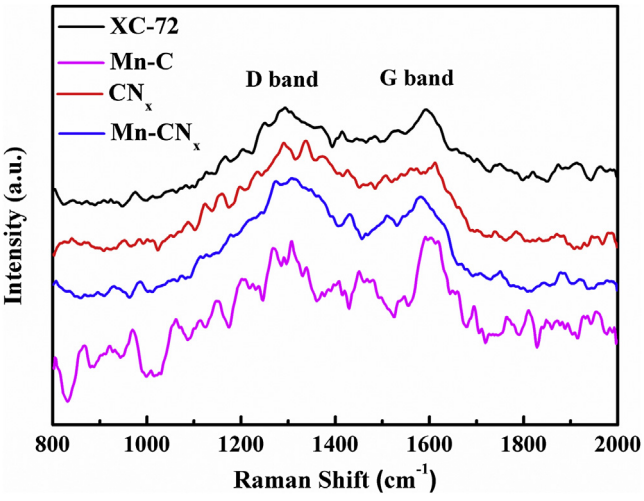

Fig. 2. Raman spectra of Mn-CN_x, CN_x, Mn–C, and XC-72.

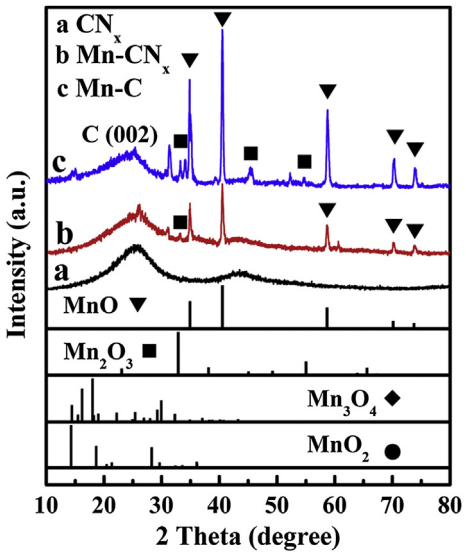

Fig. 3. X-ray diffraction patterns of Mn-CN_x, CN_x, and Mn–C.

3. Results and discussion

The SEM image in Fig. 1 shows the irregular morphology of the as-prepared Mn-CN_x particles. The size of Mn-CN_x particles ranges between 1 μm and 5 μm, on which many small particles (from 30 nm to 300 nm) are loaded on their generally smooth surface.

The graphitization degree of as-prepared Mn-CN_x, CN_x, and Mn–C were studied by Raman spectroscopy. For comparison, Raman spectroscopy of XC-72 was also presented here. Raman spectra of the all samples (Fig. 2) show two major peaks corresponding to the D-band at ~1300 cm^{-1} and G-band at ~1590 cm^{-1}. The D-band becomes active due to a reduction of symmetry near or at the crystalline edges, which is ascribed to the finite-sized crystals of graphite. The G-band is attributed to all sp^2 bonds of graphitic network [35]. The intensity ratio of the D band to G band (I_D/I_G) can be used to measure the extent of disorder in the graphitic carbon, and a higher I_D/I_G indicates more defects existed on the support [36]. The I_D/I_G of Mn-CN_x, CN_x, Mn–C, and XC-72 were 1.15, 1.14, 0.93 and 1.00 respectively, showing Mn-CN_x contained higher defect content than other samples.

Table 1
Chemical states, binding energies (BE) and area ratios (AR) of Mn-CN_x by XPS.

Elements	Chemical states	BE (eV)	AR (%)
C 1s	C–C	284.7	69.3
	C–O/C–N	285.6	26.4
	C=O	288.2	4.3
N 1s	Pyridinic N	398.3	32.4
	Pyrolic N	399.7	21.0
	Graphitic N	401.0	31.2
	Oxygenated N	402.6	15.4
Mn $2p_{3/2}$	MnO	641.0	26.1
	Mn_2O_3	641.8	26.5
	MnO_2	642.8	47.4

Fig. 3 shows the X-ray diffraction (XRD) patterns of Mn-CN_x, CN_x, and Mn–C. For comparison, the diffraction peaks and relative intensities of MnO, Mn_2O_3, Mn_3O_4 and MnO_2 are also presented in this figure. Three samples showed the peak located at ca. 24°, which is related to the diffraction peak of carbon (002). Both Mn-CN_x and Mn–C samples produced peaks located at 34.6°, 40.5°, 58.5°, 70.2° and 73.6°, which are attributed to the (111), (200), (220), (311) and (222)

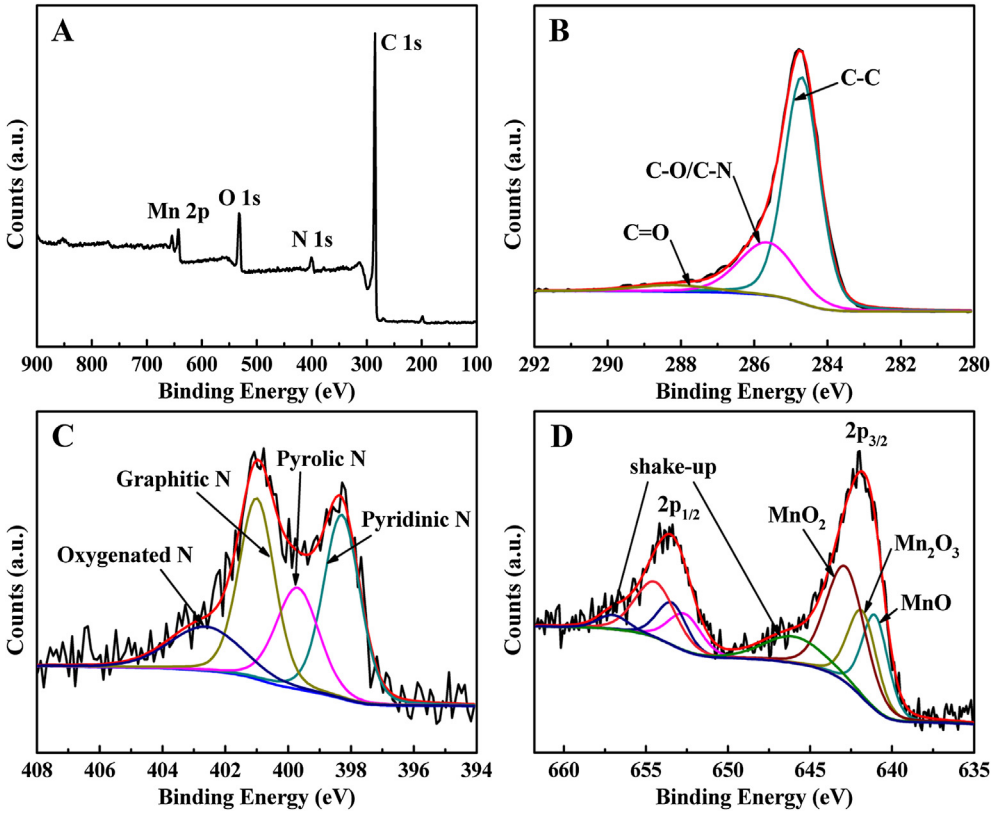

Fig. 4. XPS survey (A), high resolution C 1s (B), N 1s (C), and Mn 2p (D) spectra of Mn–CN_x.

crystal facets of MnO, respectively. The diffraction peaks ascribed to Mn_2O_3 at 33.1° occurred in both Mn-CN_x and Mn–C, while the major manganese oxide component in both samples appears to be MnO.

X-ray photoelectron spectroscopy (XPS) was used to determine the chemical composition of the materials. Fig. 4 shows the XPS spectra of Mn-CN_x. In the XPS survey of Mn-CN_x, the elements C, N, O and Mn were detected, which confirmed that N and Mn atoms existed in Mn-CN_x after the two-step carbonization. The high-resolution C 1s XPS spectrum (Fig. 4B) of Mn-CN_x shows a new peak at 286 eV, which results from carbon atoms bonded with

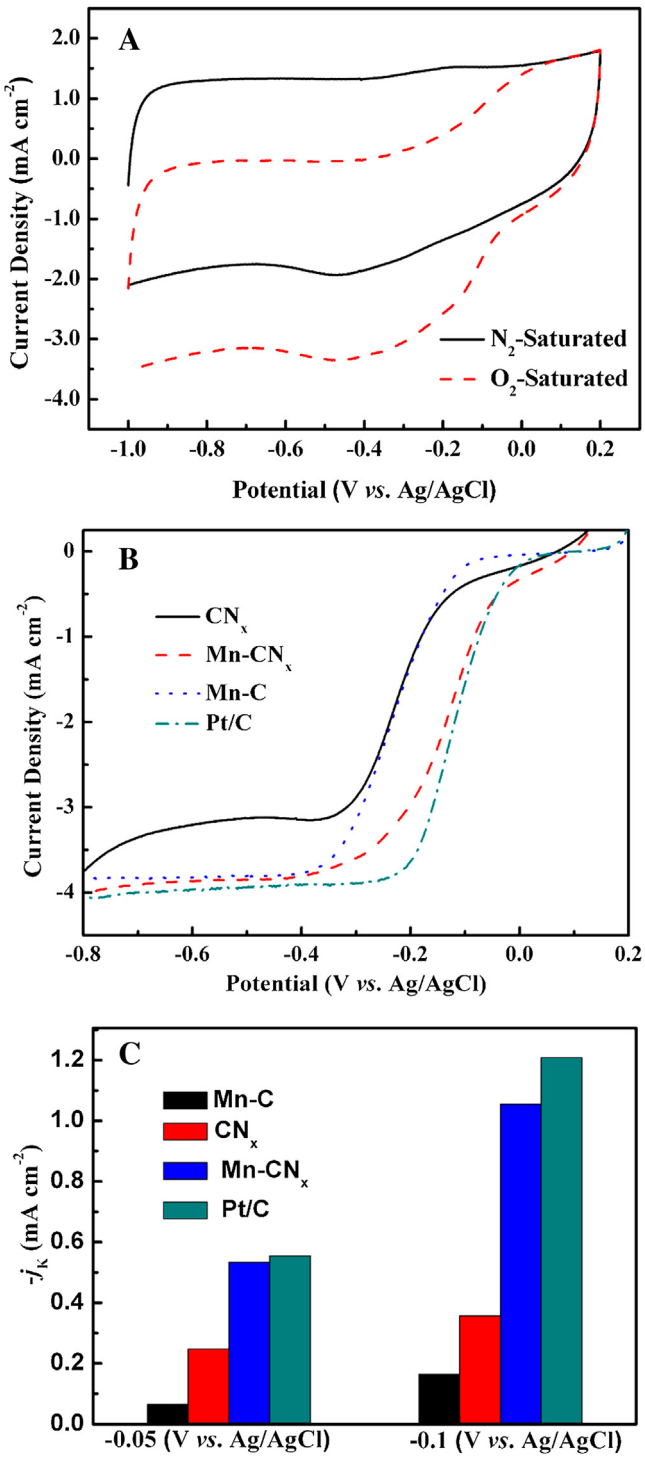

Fig. 5. (A) Cyclic voltammetry curves of Mn-CN_x electrode in nitrogen- and oxygen-saturated 0.1 M KOH aqueous electrolyte solutions. The scan rate was 50 mV s^{-1}. (B) LSV curves for CN_x, Mn-CN_x, Mn–C and commercial Pt/C catalysts on a glassy carbon rotating disk electrode saturated in O_2 at a rotation rate of 1600 rpm the loading of CN_x, Mn-CN_x, Mn–C is 0.816 mg cm^{-2}. (C) The kinetic current derived of figure B of the four catalysts at −0.05 and −0.1 V, respectively.

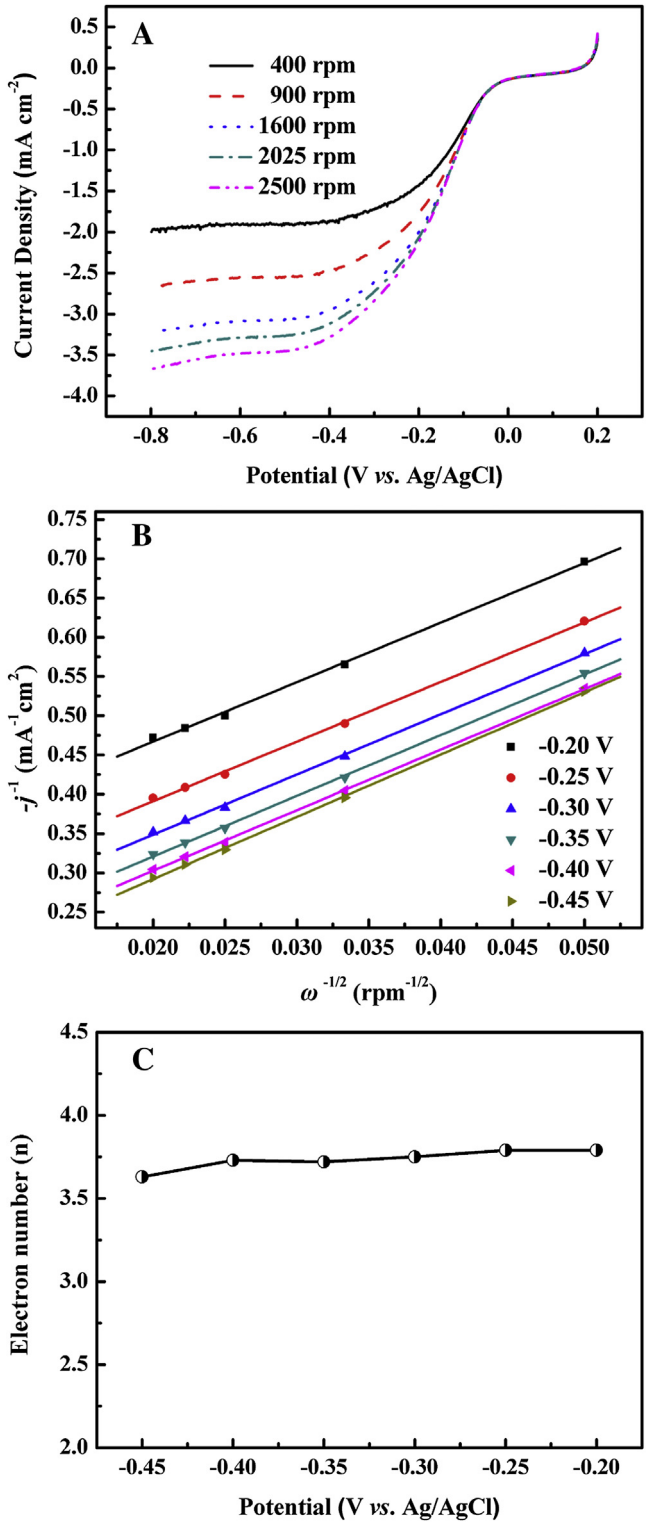

Fig. 6. (A) LSV curves for Mn-CN_x in O_2-saturated 0.1 M KOH solution at a scan rate of 5 mV s^{-1} and various rotation rates. (B) Koutecky–Levich plots of Mn-CN_x at different electrode potentials. (C) The dependence of electron transfer number *n* on the potential.

other hetero-atoms, such as O and N. Peak deconvolution was carried out to fit the C 1s spectra into three components, namely: sp^2 C (284.7 eV), C–O/C–N (285.6 eV), and C=O (288.20 eV) [37,38]. Since the intensities of the XPS peaks relates to the amount of C species, the atomic amount of different states of C could be calculated, revealing that 69.3% of C was graphite, 26.4% was C–O/C–N bonds and 4.3% was C=O bonds. The N 1s spectrum was very useful for analyzing the nature of N functionalities in Mn-CN_x. It has been reported there are four types of nitrogen species present in carbon-based materials, such as coal and charcoal. The N 1s spectrum for Mn-CN_x (Fig. 4C) can be fitted into four N entities, which are pyridinic nitrogen, pyrrolic nitrogen, graphitic nitrogen and oxygenated nitrogen, with binding energies of 398.3, 399.7, 401.0 and 402.6 eV, respectively [16,20,24,39,40]. The total N content in Mn-CN_x materials was measured to be 4.8%, and the relative surface nitrogen amounts of pyridinic N, pyrolic N, graphitic N and oxygenated N are 32.4, 21.0, 31.2, and 15.4%, respectively. Pyridinic-N had the highest content over the other three types of N in Mn-CN_x. Pyridinic-N can provide one *p*-electron to the aromatic π-systems, which has a pair of electrons in the plane of the carbon matrix, which could increase the electron-donor property of the catalyst and enhance its electrochemical performance.

Fig. 4D shows the Mn 2p spectra of Mn-CN_x. The Mn 2p spectrum can be deconvoluted into three pairs of doublets and two other satellite peaks [41,42]. The first doublet at 641.0 and 652.6 eV corresponds to Mn $2p_{3/2}$ and Mn $2p_{1/2}$, characteristic of MnO. Two shake-up satellite peaks were observed at 646.0 eV and 657.0 eV, which confirmed the presence of MnO. The second doublet (at 641.8 and 653.4 eV), with a binding energy (BE) of 0.8 eV higher than MnO, could be assigned to Mn^{3+} species in Mn_2O_3. The third doublet, which is the strongest in terms of intensity and at even higher bond energy (at 642.8 and 654.4 eV), was caused by a large amount of MnO_2 on the surface [43,44]. A comparison of the relative areas (Table 1) of integrated intensity of MnO, Mn_2O_3, and MnO_2 shows that the MnO_2 of the Mn species on the surface was predominately metallic (47.4%).

The electrocatalytic activity of Mn-CN_x was first evaluated by ORR using a three-electrode electrochemical station. Fig. 5 shows cyclic voltammograms (CVs) for the Mn-CN_x electrode in both N_2- and O_2-saturated 0.1 M KOH solutions. In N_2-saturated KOH solution, no clear current peak was observed in the potential range from −1.0 to 0.2 V. In the O_2-saturate KOH solution, a broad cathodic current at −0.4 V occurred showing that the Mn-CN_x had

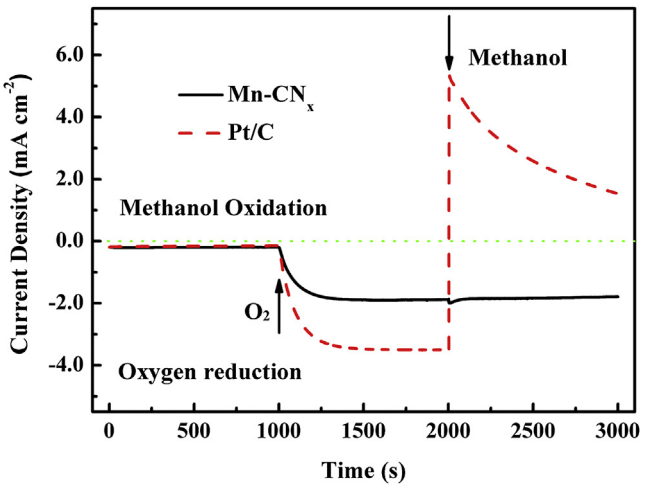

Fig. 7. Current-time response of Mn-CN_x and commercial Pt/C at −0.26 V in 0.1 M KOH saturated with N_2 (0–1000 s), and O_2 (1000–2000 s), and in O_2-saturated 3 M CH_3OH (2000–3000 s).

catalytic activity for ORR. The electrocatalytic activities of CN_x, Mn-CN_x and commercial Pt/C (20 wt%, J.M. Corp.) were then studied by the linear sweep voltammetry (LSV) curves in O_2-saturated 0.1 M KOH aqueous solution using a rotating disk electrode (Fig. 5B). CN_x and Mn-CN_x were thus benchmarked against the ORR activity of commercial Pt/C. Mn–C and CN_x electrodes showed ORR activity. Mn-CN_x displayed more positive onset potential for ORR than Mn–C and CN_x, indicating a significant enhancement of ORR catalytic activity occurred through the introduction of Mn species into CN_x. the result suggested that the enhanced activity of Mn-CN_x relates to the synergistic effect of Mn, N and C, where chemical interaction between the Mn and the CN_x formed during the heat-treatment improves catalyst efficiency and facilitates charge transfer. In addition, the half-wave potential of Mn-CN_x was only 12 mV lower than that of commercial Pt/C.

The kinetic current (j_K) was calculated by K–L equations [44] from the ORR polarization curve by mass-transport correction and normalized to the geometric area of the electrode.

$$\frac{1}{j} = \frac{1}{j_K} + \frac{1}{j_L} \tag{1}$$

in which j is the measured current density, j_K and j_L are the kinetic and diffusion-limiting current densities. As shown in Fig. 5C, Mn-CN_x exhibited an activity of 0.534 mA cm^{-2} at −0.05 V and 1.055 mA cm^{-2} at −0.1 V, respectively. It shows that the activity of Mn-CN_x for ORR is much higher than that of Mn–C and CN_x, and comparable to that of Pt/C.

To further understand the role of Mn-CN_x in ORR activity, the reaction kinetics was investigated using rotating disk electrode (RDE) voltammetry. The voltammetric profiles in O_2-saturated 0.1 M KOH solution (Fig. 6A) show that the current density increased with increasing rotation rates from 400 to 2500 rpm. The onset potential for the ORR on Mn-CN_x was approximately −0.02 V. The corresponding Koutecky–Levich (K–L) plots show good linearity (Fig. 6B). The slopes remain approximately constant in the potential range from −0.20 to −0.45 V, which suggests a similar electron-transfer number per O_2 molecule was involved in O_2 reduction. The linearity and parallelism of the plots usually indicate first-order reaction kinetics with respect to the concentration of dissolved O_2. The kinetic parameters can be analyzed on the basis of the K–L equations [44]:

$$\frac{1}{j} = \frac{1}{j_K} + \frac{1}{j_L} = \frac{1}{j_K} + \frac{1}{B\omega^{0.5}} \tag{2}$$

in which j is the measured current density, j_K and j_L are the kinetic and diffusion-limiting current densities, ω is the angular velocity of the disk, and B is related to the diffusion-limiting current density:

$$B = 0.2nF(D_{o_2})^{2/3}\nu^{-1/6}C_{o_2} \tag{3}$$

where n is the number of electrons exchanged per oxygen molecule, F is the Faraday constant (96485 C mol^{-1}), D_{o_2} is the oxygen diffusion coefficient (1.9×10^{-5} cm^2 s^{-1}), ν is the kinematic viscosity of the electrolyte (1.13×10^{-2} cm^2 s^{-1}), and C_{o_2} is the bulk concentration of oxygen (1.2×10^{-3} mol L^{-1}). The constant 0.2 is adopted when the rotation speed is expressed in rpm. The dependence of n on the potential at Mn-CN_x electrode is shown in Fig. 6C, and n was calculated to be 3.74 on average. This indicates a four-electron transfer reaction occurred to reduce O_2 directly to OH^- similar to the commercial Pt/C electrode, and thus effective ORR process.

To examine ORR selectivity on Mn-CN_x, a methanol crossover test on the catalysts was carried out using current–time

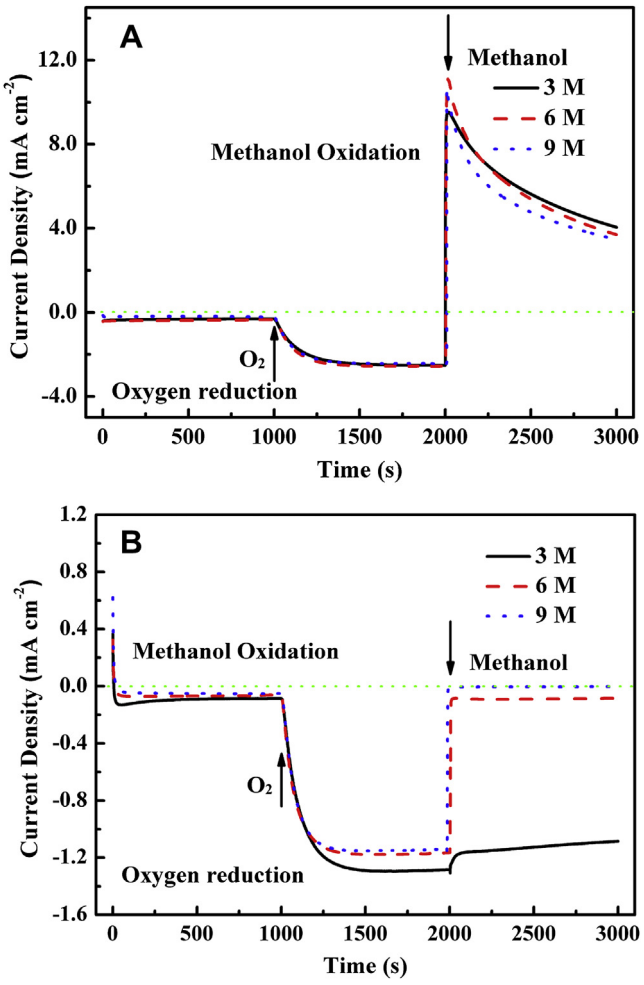

Fig. 8. Current–time response of Mn-CN_x and commercial Pt/C at −0.15 V in 0.1 M KOH saturated with N_2 (0–1000 s), and O_2 (1000–2000 s), and in O_2-saturated 3, 6, and 9 M CH_3OH (2000–3000 s), respectively.

measurements with a rotation rate of 1600 rpm. Fig. 7 shows the corresponding response at a constant potential of −0.26 V for 3000 s in a 0.1 M KOH solution first saturated with N_2 (0–1000 s), followed by introduction of O_2 (1000–2000 s) into the solution, and addition of methanol to yield an O_2-saturated 3 M CH_3OH during 2000–3000 s. The ORR current of Mn-CN_x did not show any significant change after the addition of methanol indicating that methanol had minimal effect on ORR performance. For commercial Pt/C, the corresponding current shifted from a cathodic current to a reversed anodic current in a very short time after the addition of methanol, indicating a conversion from oxygen reduction to methanol oxidation. Compared to commercial Pt/C, Mn-CN_x had far greater tolerance to methanol crossover because the ORR potential on Mn-CN_x was much lower than that for oxidation of fuel molecules.

In addition, a methanol crossover test on the catalysts at different methanol concentrations at a constant potential of −0.15 V was also carried out using current-time measurements with a rotation rate of 1600 rpm, the obtained results were plotted as Fig. 8. For commercial Pt/C shown in Fig. 8A, a reversed anodic current appears once the addition of methanol. In the case of Mn-CN_x, a reversed anodic current can't be observed, even if the methanol concentration reached 9 M. These results again demonstrated that Mn-CN_x has inertia toward MOR.

4. Conclusions

A highly active, low cost ORR electrocatalyst derived from glycine and manganese salts was successfully prepared via a facile method with a two-step carbonizing process. The results show that the catalytic ORR activity was greatly enhanced by introducing Mn atoms into nitrogen-doped carbon. Compared with Mn–C and CN_x, Mn-CN_x had outstanding ORR performance due to synergy among Mn, N and C. Although the ORR activity of Mn-CN_x was slightly lower than that of commercial Pt/C, it had excellent durability in the methanol. Mn-CN_x is therefore a promising alternative to commercial Pt/C for ORR in alkaline solution due to its comparative ORR activity, much better selectivity in the fuel, low cost and easy synthesis.

Acknowledgments

The authors would like to thank the National Natural Science Foundation of China (21163018, 21363022, and 51362027) for financially supporting this work.

References

[1] D. Strmcnik, M. Escudero-Escribano, K. Kodama, V.R. Stamenkovic, A. Cuesta, N.M. Markovi&cacute, Nat. Chem. 2 (2010) 880–885.
[2] J. Suntivich, H.A. Gasteiger, N. Yabuuchi, H. Nakanishi, J.B. Goodenough, Y. Shao-Horn, Nat. Chem. 3 (2011) 546–550.
[3] R.F. Wang, K.L. Wang, H. Wang, Q.Z. Wang, J. Key, V. Linkov, S. Ji, Int. J. Hydrogen Energy 38 (2013) 5783–5788.
[4] R.F. Wang, J.C. Jia, H. Wang, Q.Z. Wang, S. Ji, Z.Q. Tian, J. Solid State Electrochem. 17 (2013) 1021–1028.
[5] B. Lim, M. Jiang, P.H. Camargo, E.C. Cho, J. Tao, X. Lu, Y. Zhu, Y. Xia, Science 324 (2009) 1302–1305.
[6] J. Greeley, I. Stephens, A. Bondarenko, T.P. Johansson, H.A. Hansen, T. Jaramillo, J. Rossmeisl, I. Chorkendorff, J.K. Nørskov, Nat. Chem. 1 (2009) 552–556.
[7] D. Yu, E. Nagelli, F. Du, L. Dai, J. Phys. Chem. Lett. 1 (2010) 2165–2173.
[8] S. Xu, L. Yong, P. Wu, ACS Appl. Mater. Interfaces 5 (2013) 654–662.
[9] C.-L. Lee, C.-C. Syu, Int. J. Hydrogen Energy 36 (2011) 15068–15074.
[10] H.-C. Huang, I. Shown, S.-T. Chang, H.-C. Hsu, H.-Y. Du, M.-C. Kuo, K.-T. Wong, S.-F. Wang, C.-H. Wang, L.-C. Chen, Adv. Funct. Mater. 22 (2012) 3500–3508.
[11] F. Yin, K. Takanabe, M. Katayama, J. Kubota, K. Domen, Electrochem. Commun. 12 (2010) 1177–1179.
[12] H.-J. Zhang, H.-C. Kong, X. Yuan, Q.-Z. Jiang, J. Yang, Z.-F. Ma, Int. J. Hydrogen Energy 37 (2012) 13219–13226.
[13] W. Yang, T.-P. Fellinger, M. Antonietti, J. Am. Chem. Soc. 133 (2010) 206–209.
[14] Y. Zheng, Y. Jiao, J. Chen, J. Liu, J. Liang, A. Du, W. Zhang, Z. Zhu, S.C. Smith, M. Jaroniec, J. Am. Chem. Soc. 133 (2011) 20116–20119.
[15] C. Venkateswara Rao, Y. Ishikawa, J. Phys. Chem. C 116 (2012) 4340–4346.
[16] Y. Ma, L. Sun, W. Huang, L. Zhang, J. Zhao, Q. Fan, W. Huang, J. Phys. Chem. C 115 (2011) 24592–24597.
[17] Z. Yang, Z. Yao, G. Li, G. Fang, H. Nie, Z. Liu, X. Zhou, X.a. Chen, S. Huang, ACS Nano 6 (2011) 205–211.
[18] D.S. Su, G. Sun, Angew. Chem. 50 (2011) 11570–11572.
[19] K. Gong, F. Du, Z. Xia, M. Durstock, L. Dai, Science 323 (2009) 760–764.
[20] Z. Lin, M.-k. Song, Y. Ding, Y. Liu, M. Liu, C.-p. Wong, Phys. Chem. Chem. Phys. 14 (2012) 3381–3387.
[21] L. Qu, Y. Liu, J.-B. Baek, L. Dai, ACS Nano 4 (2010) 1321–1326.
[22] K.A. Kurak, A.B. Anderson, J. Phys. Chem. C 113 (2009) 6730–6734.
[23] Z.P. Li, Z.X. Liu, K.N. Zhu, Z. Li, B.H. Liu, J. Power Sources 219 (2012) 163–171.
[24] X. Li, G. Liu, B.N. Popov, J. Power Sources 195 (2010) 6373–6378.
[25] X. Li, B.N. Popov, T. Kawahara, H. Yanagi, J. Power Sources 196 (2011) 1717–1722.
[26] S. Mukerjee, S. Srinivasan, M.P. Soriaga, J. McBreen, J. Electrochem. Soc. 142 (1995) 1409–1422.
[27] Y. Kang, C.B. Murray, J. Am. Chem. Soc. 132 (2010) 7568–7569.
[28] S.P. Hsu, C.W. Liu, H.S. Chen, T.Y. Chen, C.M. Lai, C.H. Lee, J.F. Lee, T.S. Chan, L.D. Tsai, K.W. Wang, Electrochim. Acta 105 (2013) 180–187.
[29] Q. Jia, C.U. Segre, D. Ramaker, K. Caldwell, M. Trahan, S. Mukerjee, Electrochim. Acta 88 (2013) 604–613.
[30] W. Xiao, D. Wang, X.W. Lou, J. Phys. Chem. C 114 (2009) 1694–1700.
[31] K.L. Pickrahn, S.W. Park, Y. Gorlin, H.-B.-R. Lee, T.F. Jaramillo, S.F. Bent, Adv. Energy Mater. 2 (2012) 1269–1277.
[32] M.S. El-Deab, T. Ohsaka, Angew. Chem. 45 (2006) 5963–5966.
[33] M. Calegaro, F. Lima, E. Ticianelli, J. Power Sources 158 (2006) 735–739.
[34] I. Roche, E. Chaînet, M. Chatenet, J. Vondrák, J. Phys. Chem. C 111 (2007) 1434–1443.
[35] R. Nemanich, S. Solin, Phys. Rev. B 20 (1979) 392–401.
[36] J.C. Jia, R.F. Wang, H. Wang, S. Ji, J. Key, V. Linkov, K. Shi, Z.Q. Lei, Catal. Commun. 16 (2011) 60–63.

[37] X.-W. Zhou, R.-H. Zhang, Z.-Y. Zhou, S.-G. Sun, J. Power Sources 196 (2011) 5844–5848.
[38] S. Wang, D. Yu, L. Dai, D.W. Chang, J.-B. Baek, ACS Nano 5 (2011) 6202–6209.
[39] K.L. Wang, H. Wang, S. Ji, H.Q. Feng, V. Linkov, R.F. Wang, RSC Adv. 3 (2013) 12039–12042.
[40] T.B. Tian, H. Wang, J. Key, S. Ji, V. Linkov, R.F. Wang, RSC Adv. 3 (2013) 16949–16953.
[41] W.-J. Hong, S. Iwamoto, S. Hosokawa, K. Wada, H. Kanai, M. Inoue, J. Catal. 277 (2011) 208–216.
[42] M. Kostowskyj, D. Kirk, S. Thorpe, Int. J. Hydrogen Energy 35 (2010) 5666–5672.
[43] Y. Cao, H. Yang, X. Ai, L. Xiao, J. Electroanal. Chem. 557 (2003) 127–134.
[44] S. Wang, D. Yu, L. Dai, J. Am. Chem. Soc. 133 (2011) 5182–5185.